RAA 2017 Vol. **17** No. **6**, 57 (12pp) doi: 10.1088/1674–4527/17/6/57

http://www.raa-journal.org *http://iopscience.iop.org/raa*

Research in Astronomy and Astrophysics

Searching for initial stage of massive star formation around the H II region G18.2–0.3

Chuan-Peng Zhang, Jing-Hua Yuan, Jin-Long Xu, Xiao-Lan Liu, Nai-Ping Yu, Nan Li, Li-Ping He, Guo-Yin Zhang and Jun-Jie Wang

National Astronomical Observatories, Chinese Academy of Sciences, Beijing 100012, China; *cpzhang@nao.cas.cn*
Received 2016 November 3; accepted 2017 March 7

Abstract Sometimes, early star formation can be found in cold and dense molecular clouds, such as an infrared dark cloud. Considering that star formation often occurs in clusters, H II regions may be triggering a new generation of star formation, so we can search for the initial stage of massive star formation around H II regions. Based on the above, this work introduces one method to search for the initial stage of massive star formation around H II regions. Towards one section of the H II region G18.2–0.3, multiwavelength observations are carried out to investigate its physical properties. Through analysis, we find three potential initial stages of massive star formation, suggesting that it is feasible to use in searching for the initial stage of massive star formation around H II regions.

Key words: infrared: stars — stars: formation — initial stage — H II regions

1 INTRODUCTION

High-mass star formation played an important role in forming the Milky Way (Whitworth et al. 1994; Fuller et al. 2005). Regions of massive star formation are on average more distant than the sites of low-mass star formation. The early stage of clustered star formation is characterized by dense, parsec-scale filamentary structures interspersed with complexes of dense cores (< 0.1 pc cores clustered in complexes separated by $\sim$1 pc) with masses from about 10 to 100 $M_\odot$ (Battersby et al. 2014). So far, we still have poor knowledge about the process of early high-mass star formation, due to the initial stage of high-mass star formation being one of the most difficult processes to detect and study by current instruments (Motte et al. 2007; Pillai et al. 2007, 2011). Another reason is that we do not have enough of a sample in the prestellar stage. Therefore, to get more samples we propose one method of searching for the initial stage of massive star formation around H II regions.

Infrared dark clouds (IRDCs) are often suggested as the precursors to massive stars and stellar clusters (Rathborne et al. 2007, 2010; Sanhueza et al. 2012; Jiménez-Serra et al. 2014; Wang et al. 2014). Lots of studies (e.g., Rathborne et al. 2007, 2010; Zhang et al. 2017) about IRDCs have focused on the earliest example of massive star formation. However, other conditions can also breed young stellar objects (YSOs), such as surrounding H II regions and supernova remnants (SNRs). H II regions are manifestations of newly formed massive stars that are still embedded in their natal molecular clouds (Walsh et al. 1997; Pomarès et al. 2009; Zhang et al. 2014). Dust in the molecular cloud renders H II regions observable only at radio, infrared and submillimeter wavelengths (Churchwell 2002). The central star of an H II region is believed to have ceased accreting matter and to have settled down for a short lifetime on the main sequence (Hofner et al. 2002). In addition, H II regions are almost always accompanied by molecular clouds on their borders. The Orion Nebula, for example, is merely a conspicuous ionized region on the nearby face of a much larger dark cloud; the H II region is almost entirely produced by the ionization provided by a single hot star (Walsh et al. 1997; Churchwell 2002; Pomarès et al. 2009). Studies of infrared dust bubbles associated with H II regions have revealed some triggered star formation in a ringlike shell (e.g., Zhang & Wang 2012, 2013; Zhang et al. 2013, 2016; Yuan et al. 2014).

The goal of this work is to introduce one method of searching for examples of the initial stage of massive star formation around the H II region G18.2–0.3, which has an area of $0.4^\circ \times 0.4^\circ$ centered at $l = 18.2^\circ$, $b = -0.3^\circ$

(see Figs. 1 and 2). The H II region G18.2–0.3 consists of the SNR G18.1–0.1 (Green 2009), infrared dust bubbles N21 and N22 (Churchwell et al. 2006), and the H II regions G018.149–00.283 (Kolpak et al. 2003), G18.197–00.181 (Lockman 1989) and G18.237–0.240 (Paron et al. 2013). The distance is around 4 kpc (Paron et al. 2013). This target is selected based on the fact that massive stars are usually born in clusters, probably from material of the same molecular cloud, which then produce, along their evolution, neighboring H II regions, interstellar bubbles and SNRs that can interact with the parental cloud (Paron et al. 2013).

In this work, multiwavelength observations are carried out to investigate the physical properties of the H II region G18.2–0.3. The molecular line ^{13}CO (1–0) and dust continuum including 8.0, 70, 870 μm, 21 cm and *Herschel* data are adopted to study the H II region. This paper is arranged as follows. Section 2 presents the data used in this work. Section 3 shows the results of the data analysis. In Section 4, we discuss how to search for examples of the initial stage of massive star formation around a clearly identified H II region complex, the associations of the initial stage of massive star formation with H II regions nearby and properties of associated massive star formation. Finally, a summary is presented in Section 5.

2 ARCHIVAL DATA

2.1 Dust Continuum

The combined dust continuum data are comprised of *Spitzer* InfraRed Array Camera (IRAC) 8.0 μm (1σ = 78 μJy; Benjamin et al. 2003; Churchwell et al. 2009). The resolution at 8.0 μm is $\sim$ $2.0''$. IRAC is one of three focal plane instruments on the *Spitzer Space Telescope*.[1] IRAC is a four-channel camera that provides simultaneous $5.2' \times 5.2'$ images at 3.6, 4.5, 5.8 and 8.0 μm. The Multiband Imaging Photometer for *Spitzer* (MIPS) produced imaging and photometry in three broad spectral bands, centered nominally at 24, 70 and 160 μm, and low-resolution spectroscopy between 55 and 95 μm. The resolution at 24 μm is $\sim$ $6''$. The *Herschel Space Observatory*[2] is a 3.5 meter telescope observing the far-infrared and submillimeter Universe. The imaging bands for the Photo detector Array Camera and Spectrometer (PACS) are centered at 70, 100 and 160 μm ($1\sigma_{70\,\mu\rm m}$ = $20\,\rm MJy\,sr^{-1}$, $1\sigma_{160\,\mu\rm m}$ = $20\,\rm MJy\,sr^{-1}$; Poglitsch et al. 2010; Molinari et al. 2016). The resolution at 70 and 160 μm is about $8.4''$ and $13.5''$, respectively. The Spectral and Photometric Imaging Receiver (SPIRE) 250, 350 and 500 μm ($1\sigma_{250\,\mu\rm m}$ = 10 $\rm MJy\,sr^{-1}$, $1\sigma_{350\,\mu\rm m}$ = 4 $\rm MJy\,sr^{-1}$ and $1\sigma_{500\,\mu\rm m}$ = 2 $\rm MJy\,sr^{-1}$; Griffin et al. 2010; Molinari et al. 2016) bands have a spatial resolution of about $18.1''$, $24.9''$ and $36.4''$, respectively. ATLASGAL[3] 870 μm (1σ = $54\,\rm mJy\,beam^{-1}$; Schuller et al. 2009; Csengeri et al. 2014) is the APEX Telescope Large Area Survey of the Galaxy, an observing program with the LABOCA bolometer array at APEX, located at an altitude of 5100 m on Chajnantor, Chile. Its spatial resolution at 870 μm is about $19''$. The radio continuum data at 21 cm, with a synthesized beam of about $45''$, were extracted from observations for the 1.4 GHz NRAO VLA Sky Survey (NVSS; Condon et al. 1998).

2.2 Molecular Line

The molecular line data are accessed from the Milky Way Galactic Ring Survey (GRS), which was performed by a Boston University and Five College Radio Astronomy Observatory (FCRAO) collaboration (Jackson et al. 2006). Using the SEQUOIA multi-pixel array receiver on the FCRAO 14 m telescope, a ^{13}CO (1–0) survey of the inner Galaxy was conducted. The GRS offers a sensitivity of < 0.4 K, spectral resolution of 0.2 $\rm km\,s^{-1}$ and angular resolution of $46''$ with sampling $22''$. The original intensities are on antenna temperature scale $T_{\rm A}^*$. To convert this to main beam temperature $T_{\rm MB}$, $T_{\rm A}^*$ is divided by the main beam efficiency of 0.48. The GILDAS[4] software package was used to reduce the molecular line data.

3 ANALYSIS

3.1 Clump Extraction

The typical terminology (e.g., Bergin & Tafalla 2007) defines a clump as having a physical size of 0.3–3 pc with a mass of about 50–500 $M_\odot$. Therefore, based on the derived effective radius in Table 1, the extracted objects are called clumps in this work.

Potentially massive clumps are extracted with the *Gaussclumps* procedure (Stutzki & Guesten 1990; Kramer et al. 1998) in the GILDAS software package from a 870 μm map, assuming that the flux density of each clump follows a Gaussian distribution.

[1] This work is based partly on observations made with the which is operated by the Jet Propulsion Laboratory, California Institute of Technology under a contract with NASA.

[2] *Herschel* is an ESA space observatory with science instruments provided by European-led Principal Investigator consortia and with important participation from NASA.

[3] The ATLASGAL project is a collaboration between the Max-Planck-Gesellschaft, the European Southern Observatory (ESO) and the Universidad de Chile.

[4] *http://www.iram.fr/IRAMFR/GILDAS/*

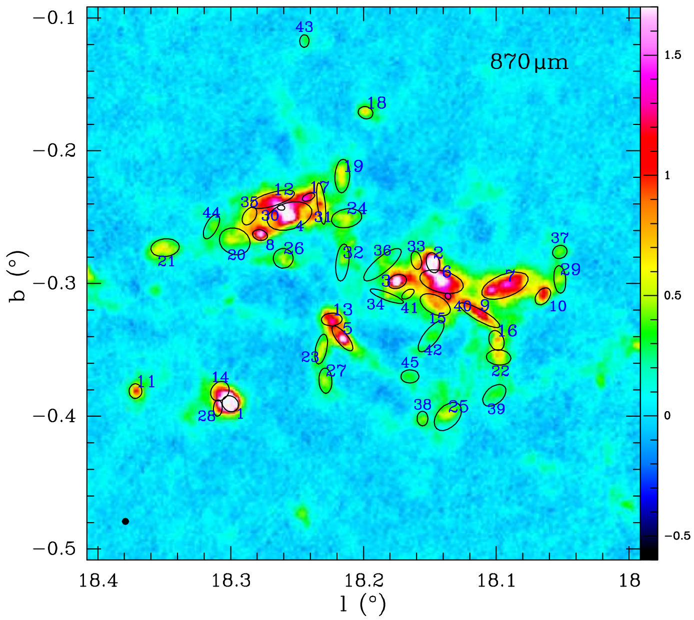

Fig. 1 870 μm dust continuum emission overlaid by the extracted Gaussian clumps for the H II region G18.2–0.3. The unit of the 870 μm color bar is in $\mathrm{Jy\,beam^{-1}}$. The beam size is indicated at the bottom-left corner.

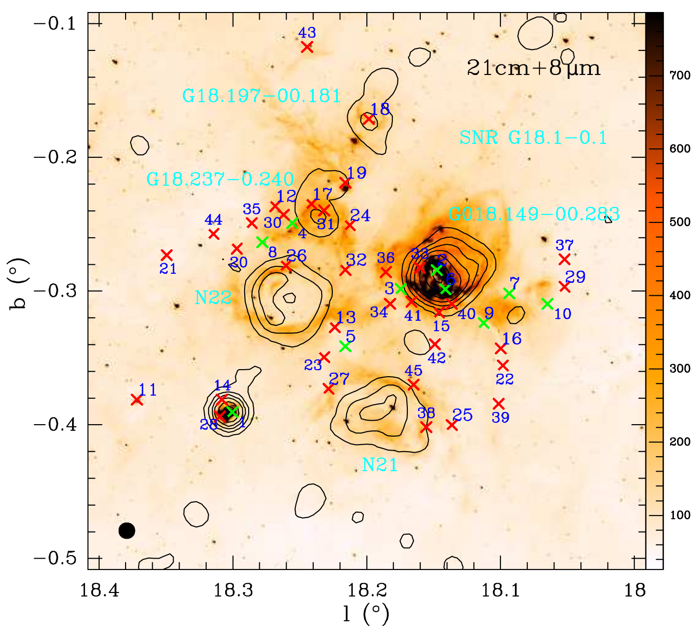

Fig. 2 21 cm continuum contours superimposed on an image of 8 μm emission for the H II region G18.2–0.3. Several H II regions are indicated with their names. The associated contour levels of the 21 cm emission are 3σ, 20σ, 50σ, 100σ, 200σ, 350σ and 520σ with σ = 0.002 $\mathrm{Jy\,beam^{-1}}$. The unit of the 8 μm color bar is in $\mathrm{MJy\,sr^{-1}}$. The crosses with numbers indicate peak positions of extracted massive clumps (see Fig. 1). The green crosses show the 10 most massive clumps.

Gaussclumps can be used to fit a two-dimensional clump locally to the maximum of the input cube. It then subtracts this clump from the cube, creating a residual map, and then continues with the maximum of this residual map. This procedure is repeated until a stop criterion is met, for instance when the maximum of the residual maps drops below the 3σ level. We just consider the clumps to have peak intensity of 870 μm emission above 6σ. The measured parameters are also listed in Table 1, and clump sizes are displayed in Figure 1, and also with crosses in Figure 2. The measured FWHMx and FWHMy have been convolved with beam size.

Table 1 Parameters of Extracted Clumps

No.	Offset-x	Offset-y	Distance	$I_{870\,\mu\mathrm{m}}$	FWHMx	FWHMy	R_{eff}	T_{dust}	$N_{\mathrm{H_2}}$	Mass	Lum.
	($''$)	($''$)	(kpc)	(Jy beam^{-1})	($''$)	($''$)	(pc)	(K)	(cm^{-2})	($M_\odot$)	($L_\odot$)
(1)	(2)	(3)	(4)	(5)	(6)	(7)	(8)	(9)	(10)	(11)	(12)
1	361.00	–325.78	3.22 ± 0.20	4.06	46.47	40.71	0.34	30.4	2.54E+22	717	39185
2	–188.47	56.70	3.52 ± 0.23	3.08	56.13	35.96	0.38	30.0	1.99E+22	442	46717
3	**–91.60**	**5.75**	$\mathbf{3.40 \pm 0.19}$	**2.23**	**51.63**	**36.80**	**0.36**	**23.1**	**1.90E+22**	**405**	**16746**
4	200.44	183.52	4.92 ± 0.28	2.22	95.34	62.25	0.92	24.7	1.76E+22	1411	34990
5	**57.24**	**–148.65**	$\mathbf{3.40 \pm 0.19}$	**1.80**	**83.31**	**30.06**	**0.41**	**14.7**	**8.27E+22**	**1243**	**5256**
6	–211.70	5.40	3.52 ± 0.23	1.74	91.04	59.00	0.63	31.7	1.49E+22	1108	100109
7	–383.42	–5.90	3.45 ± 0.20	1.46	98.13	60.93	0.65	21.8	2.18E+22	1325	28660
8	**280.40**	**131.60**	$\mathbf{4.92 \pm 0.28}$	**1.43**	**41.16**	**28.44**	**0.41**	**22.2**	**1.23E+22**	**219**	**3705**
9	–314.69	–85.81	3.52 ± 0.23	1.21	55.52	29.84	0.35	24.2	1.17E+22	294	7963
10	–486.34	–34.27	3.40 ± 0.19	1.11	52.32	34.65	0.35	21.3	1.30E+22	295	4045
11	617.90	–291.80	3.36 ± 0.18	1.03	39.90	34.39	0.30	23.6	1.06E+22	252	3702
12	246.07	228.85	3.45 ± 0.20	0.98	84.07	36.55	0.46	21.2	1.77E+22	802	9845
13	85.82	–97.22	3.40 ± 0.19	0.90	56.42	34.91	0.37	20.9	1.86E+22	561	7053
14	389.10	–291.83	3.22 ± 0.20	0.85	56.43	46.55	0.40	26.1	2.46E+22	870	31342
15	–194.52	–57.25	3.45 ± 0.20	0.80	88.83	49.44	0.55	26.2	1.07E+22	772	38883
16	–360.47	–154.53	3.52 ± 0.23	0.74	56.03	39.06	0.40	20.4	1.25E+22	467	4788
17	148.76	234.61	3.45 ± 0.20	0.73	35.63	18.85	0.22	25.9	1.27E+22	152	4829
18	–5.73	463.46	3.45 ± 0.20	0.70	40.44	32.84	0.30	26.3	6.31E+21	134	5164
19	57.23	291.80	3.52 ± 0.23	0.62	91.29	39.82	0.51	28.4	6.27E+21	331	16238
20	349.03	114.47	4.92 ± 0.28	0.60	85.59	70.99	0.93	24.1	5.58E+21	741	14289
21	537.83	97.23	4.92 ± 0.28	0.59	77.39	47.99	0.73	17.1	2.54E+22	687	5414
22	–366.17	–200.28	3.52 ± 0.23	0.58	66.77	41.72	0.45	18.4	1.75E+22	543	4130
23	114.41	–177.38	3.40 ± 0.19	0.56	82.53	30.62	0.41	22.2	7.50E+21	416	5116
24	45.78	177.34	3.45 ± 0.20	0.56	83.22	50.81	0.54	27.0	6.50E+21	431	19329
25	–228.84	–360.44	3.40 ± 0.19	0.54	89.77	57.12	0.59	22.6	6.47E+21	603	9579
26	217.41	68.65	4.92 ± 0.28	0.54	53.61	53.53	0.64	29.6	3.39E+21	208	11795
27	102.99	–263.20	3.40 ± 0.19	0.54	68.33	35.35	0.41	24.1	7.15E+21	235	6126
28	394.80	–337.58	3.22 ± 0.20	0.52	44.27	24.17	0.26	27.8	1.02E+22	296	16110
29	–532.10	11.45	3.40 ± 0.19	0.52	75.50	32.48	0.41	17.8	1.54E+22	412	3056
30	223.14	205.98	4.92 ± 0.28	0.51	25.54	20.91	0.28	23.4	2.10E+22	197	3311
31	114.43	217.43	3.45 ± 0.20	0.51	53.25	20.92	0.28	27.3	8.67E+21	162	7306
32	57.19	57.23	3.45 ± 0.20	0.48	80.62	35.17	0.45	26.1	5.30E+21	291	11778
33	–143.03	62.94	3.52 ± 0.23	0.47	50.19	27.60	0.32	31.4	6.90E+21	194	20932
34	–62.94	–34.34	3.40 ± 0.19	0.47	96.35	20.90	0.37	24.3	7.65E+21	243	6882
35	308.97	183.08	4.92 ± 0.28	0.44	53.17	32.45	0.50	21.2	1.14E+22	447	3848
36	–51.49	51.50	3.45 ± 0.20	0.43	88.75	41.03	0.50	27.6	5.45E+21	381	19025
37	–532.11	85.83	3.40 ± 0.19	0.42	39.80	35.38	0.31	17.7	1.45E+22	222	1603
38	–160.20	–366.19	3.40 ± 0.19	0.42	38.88	29.76	0.28	25.9	5.90E+21	118	3917
39	–354.74	–303.24	3.40 ± 0.19	0.41	73.45	45.71	0.48	21.2	8.40E+21	443	5025
40	–228.86	–34.33	3.45 ± 0.20	0.41	23.88	19.84	0.18	28.9	1.16E+22	85	5164
41	–120.16	–28.61	3.45 ± 0.20	0.39	38.45	19.49	0.23	27.2	6.98E+21	110	6328
42	–183.10	–143.05	3.40 ± 0.19	0.40	82.49	38.12	0.46	21.3	8.26E+21	411	7237
43	160.20	657.98	3.40 ± 0.19	0.38	33.81	25.32	0.24	23.1	6.82E+21	104	1807
44	411.95	154.48	4.92 ± 0.28	0.38	72.15	32.29	0.58	21.6	7.15E+21	260	3931
45	–125.87	–251.76	3.40 ± 0.19	0.38	49.04	35.85	0.35	25.9	5.89E+21	171	6064

Notes: The offset (0, 0) is located at the position of $l = 18.2°$, $b = -0.3°$. Clumps 3, 5 and 8 are potentially three initial stages of massive star formation.

3.2 Initial Stage of Massive Star Formation

A prestellar core is often suggested as the precursor of massive star formation. Prestellar cores represent a somewhat denser and more centrally-concentrated population of cores which are starless but self-gravitating (André et al. 2009). They are typically detected in sub-millimeter dust continuum emission and dense molecular gas tracers, often seen in absorption at mid- to far-infrared wavelengths (Tan et al. 2013; Chitsazzadeh et al. 2014; Wang et al. 2011, 2014; Cyganowski et al. 2014; Kong et al. 2016). However, prestellar cores are really difficult to detect, due to the fact that they have almost no infrared emission.

In this work, we define an infrared quiet clump as the initial stage of massive star formation. Infrared quiet clumps have all same the physical properties, such as being cold ($T < 18\,\mathrm{K}$) and dense ($n > 10^5\,\mathrm{cm}^{-3}$), just excluding low luminosity ($S_{24\,\mu\mathrm{m}} < (\frac{1.7\,\mathrm{kpc}}{D})^2 \times 15.0\,\mathrm{Jy}$; Motte et al. 2007; André et al. 2009; Russeil et al. 2010). As a potentially early stage of molecular clouds, IRDCs were discovered two decades ago as dark patches in mid-infrared images of the Galactic plane (Perault et al. 1996; Egan et al. 1998) and many studies of the physical conditions within them have been conducted recently (Pillai et al. 2006, 2007; Wyrowski 2008; Pillai et al. 2012; Zhang et al. 2017). H II regions do not represent the earliest stage of massive star formation, as is often claimed (e.g., Churchwell 2002). Star formation in the Milky Way always takes place in clusters and groups within large molecular clouds (Aikawa et al. 2005; Hennebelle & Chabrier 2008; André et al. 2009; Pagani et al. 2013). It is likely that the triggered early star formation by the H II region nearby can provide different views compared to IRDCs, such as conditions for triggering or breeding. Therefore, we will search for the initial stage of massive star formation around an H II region complex, as is the rationale for this work.

Three clumps are proposed as the potentially initial stage of massive star formation. They are, respectively, clump Nos. 3, 5 and 8 listed in Table 1, and presented in Figure 3. We further searched for compact point sources in MIPS 24 μm (Carey et al. 2009; Gutermuth & Heyer 2015), PACS 70 μm (Molinari et al. 2016) and ATLASGAL 870 μm (Csengeri et al. 2014) catalogs, and found that there exist counterparts for clump Nos. 3, 5 and 8. The counterparts at 24, 70 and 870 μm are listed in Table 2. Based on the definition of infrared quiet clumps ($S_{24\,\mu\mathrm{m}} < (\frac{1.7\,\mathrm{kpc}}{D})^2 \times 15.0\,\mathrm{Jy}$), the infrared property of clump Nos. 3, 5 and 8 meets this criterion.

3.3 Dust Temperature and Column Density

High-quality *Herschel* data cover a large wavelength range from 70 to 500 μm, making it practical to obtain dust temperature maps of the H II region via fitting the SED to the multiwavelength images on a pixel-by-pixel basis. First, we have followed Wang et al. (2015) in performing Fourier transform (FT) based on background removal. In this method, the original images were first transformed into the Fourier domain and separated into low and high spatial frequency components, and then inversely Fourier transformed back into the image domain. The low-frequency component corresponds to large-scale background/foreground emission, while the high-frequency component preserves the emission of interest. Detailed descriptions of the FT-based background removal method can be found in Wang et al. (2015). After removing the background/foreground emission, we regridded the pixels onto the same scale of $11.5''$, and convolved the images to a circular Gaussian beam with full width at half-maximum $(\mathrm{FWHM}) = 36.4''$ which corresponds to the measured beam of *Herschel* observations at 500 μm (Traficante et al. 2011). The intensities at multi-wavelengths of each pixel have been modeled as

$$S_\nu = B_\nu(T)(1 - e^{-\tau_\nu}), \tag{1}$$

where the Planck function $B_\nu(T)$ is modified by optical depth

$$\tau_\nu = \mu_{\mathrm{H}_2} m_{\mathrm{H}} \kappa_\nu N_{\mathrm{H}_2} / R_{\mathrm{gd}}. \tag{2}$$

Here, $\mu_{\mathrm{H}_2} = 2.8$ is the mean molecular weight adopted from Kauffmann et al. (2008), m_{H} is the mass of a hydrogen atom, N_{H_2} is the column density and $R_{\mathrm{gd}} = 100$ is the gas to dust ratio. The dust opacity κ_ν can be expressed as a power law of frequency with

$$\kappa_\nu = 5.0 \left(\frac{\nu}{600\,\mathrm{GHz}}\right)^\beta \mathrm{cm}^2\,\mathrm{g}^{-1}, \tag{3}$$

where $\kappa_\nu(600\,\mathrm{GHz}) = 5.0\,\mathrm{cm}^2\,\mathrm{g}^{-1}$ is adopted from Ossenkopf & Henning (1994). The dust emissivity index has been fixed to be $\beta = 1.75$ according to Battersby et al. (2011). The free parameters are the dust temperature T_{dust} and column density N_{H_2}.

The final resulting dust temperature map, which has a spatial resolution of $36.4''$ with a pixel size of $11.5''$, is shown in Figure 4. Other parameters are listed in Table 1. We have to admit that the derived dust temperatures are over-estimated due to contamination from the emission of H II regions nearby.

3.4 Luminosity

The total energy radiated from an object per second (named the Boltzmann luminosity) can be expressed by

$$L_{\mathrm{clump}} = 4\pi d^2 \Omega_{\mathrm{pix}} \sum I_{\mathrm{int}}, \tag{4}$$

where d, Ω_{pix} and I_{int} are the distance, solid angle and flow of energy out of a surface at each source, respectively. The I_{int} for each pixel can be estimated using the resultant dust temperature and column density (see Sect. 3.3). The luminosities of the sources with distance measurements were calculated by integrating the frequency-dependent intensities between 10^2 and 10^5 GHz within the Gaussian ellipses. The derived luminosities are listed in Table 1. We have to admit that the

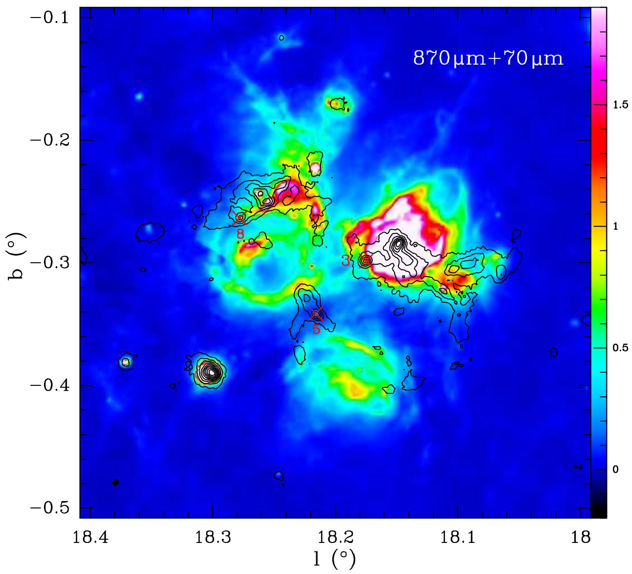

Fig. 3 870 μm dust continuum contours superimposed on an image of 70 μm emission for the H II region G18.2–0.3. The contour levels of 870 μm emission start at 6σ in steps of 8σ with $\sigma = 0.054$ Jy beam^{-1}, and its beam size is indicated at the bottom-left corner. The red crosses with numbers show three potential initial stages of massive star formation. The unit of 70 μm color bar is in MJy sr^{-1}.

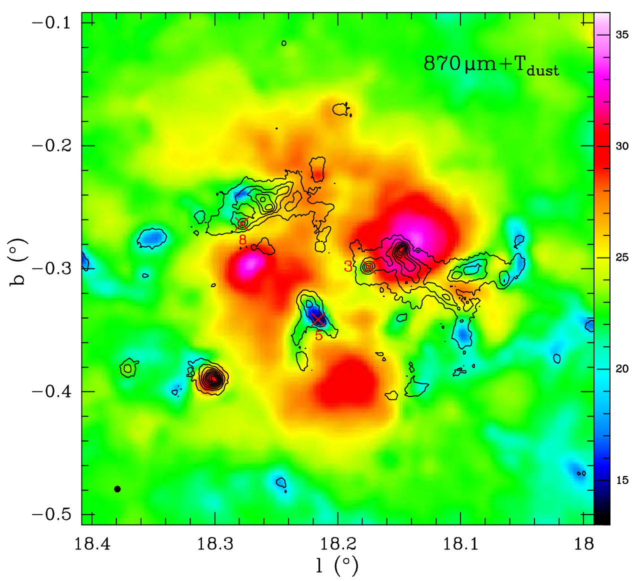

Fig. 4 870 μm dust continuum contours superimposed on an image of dust temperature $T_{\rm dust}$ for the H II region G18.2–0.3. The contour levels of 870 μm emission start at 6σ in steps of 8σ with σ = 0.054 Jy beam^{-1}, and its beam size is indicated at the bottom-left corner. The red crosses with numbers show three potential initial stages of massive star formation. The unit of the $T_{\rm dust}$ color bar is in K.

Table 2 Point Source Information at 24, 70 and 870 μm

No.	l (°)	b (°)	MIPS$_{24\,\mu\rm m}$	$S_{24\,\mu\rm m}$ (mJy)	PACS$_{70\,\mu\rm m}$	$S_{70\,\mu\rm m}$ (Jy)	ATLASGAL$_{870\,\mu\rm m}$	$S_{870\,\mu\rm m}$ (Jy)
3	18.178179	–0.299098	MG018.1751–00.2985	214.881	HIGALPB018.1782–0.2991	6.569	AGAL018.174–00.299	45.38
5	18.215827	–0.341628	MG018.2157–00.3417	773.266	HIGALPB018.2158–0.3416	3.993	AGAL018.214–00.342	9.47
8	18.276361	–0.263550	MG018.2758–00.2636	463.319	HIGALPB018.2764–0.2635	7.604	AGAL018.278–00.262	22.86

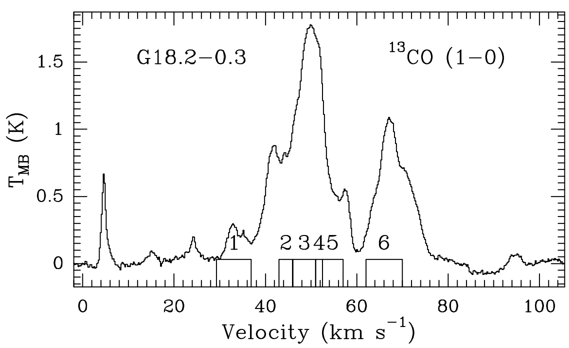

Fig. 5 Averaged ^{13}CO line within the whole H II region G18.2–0.3. The windows with numbers indicate six different velocity components (see Table 4 and Fig. 6) to be investigated further.

derived Boltzmann luminosity was also over-estimated like dust temperature due to contamination from the emission of H II regions nearby.

3.5 Clump Mass and Virial Mass

We just use *Herschel* data along with the derived dust temperatures in Section 3.3 to estimate the masses of these extracted clumps. The mass is given by the integral of column densities across the source,

$$M = \mu_{\rm H_2} m_{\rm H} d^2 \int N_{\rm H_2} d\Omega, \quad (5)$$

where d and Ω are the distance and solid angle of the source, respectively. These corresponding and derived parameters are listed in Table 1.

The virial theorem can be used to test whether one clump is in a stable state. Under the assumption of a simple spherical clump with a density distribution of ρ = constant, if ignoring magnetic fields and bulk motions of the gas (MacLaren et al. 1988; Evans 1999),

$$M_{\rm vir} \simeq 210\, r\, \Delta V^2\, (M_\odot), \quad (6)$$

where r is adopted with the clump effective radius in pc and ΔV (listed in Fig. 3) is the FWHM line width in $\rm km\,s^{-1}$. The ΔV was estimated with the ^{13}CO line. The spatial resolution of the ^{13}CO data is somewhat larger than the sizes of individual clumps, so we just considered the ^{13}CO spectrum within one pixel corresponding to the peak position of each clump. The virial parameter $\alpha_{\rm vir}$ is defined by $\alpha_{\rm vir} = M_{\rm vir}/M$. For the three identified initial stages of massive star formation, their virial masses and virial parameters are listed in Table 3. In such dense clumps, the ^{13}CO line becomes optically thick, so the virial mass is likely over-estimated.

3.6 Different Velocity Components

In Figure 5, we show the averaged ^{13}CO line within the whole H II region G18.2–0.3. The windows with numbers indicate six different velocity components (see Table 4 and Fig. 6) to be further investigated. The molecular clouds in different distances are superimposed on each other, so that we often observe different velocity components in the same line of sight.

Dust continuum has no velocity information, so we can combine molecular line ^{13}CO (1-0) to investigate the velocity correlation with the massive clumps. If the ^{13}CO (1-0) emission in different integrated-velocity ranges has good correlation with any 870 μm dust continuum distribution, its corresponding velocity information can be obtained (see Fig. 6).

Furthermore, the distances to the massive clumps were derived based on the Bayesian Distance Calculator[5] (Reid et al. 2016), which leverages these results to significantly improve the accuracy and reliability of distance estimates to other sources that are known to follow a spiral structure. Paron et al. (2013) listed the distances of several H II regions and one SNR, which are close to the derived distances with Bayesian Distance Calculator. We think that the Bayesian Distance Calculator is more reliable, so it will be adopted in this work. Based on the analysis in Figure 6, the distances of all velocity ranges for the H II region G18.2–0.3 are listed in Table 4.

In the work of Paron et al. (2013), however, the authors skipped the velocity component of [62.0 70.0] $\rm km\,s^{-1}$, which is actually associated with the H II region G18.237–0.240 and was unknown before. We have to note that the studied H II region complex G18.2–0.3 does indeed consist of many different and complicated components in the line of sight, and the H II region G18.237–0.240 (associated with the velocity component of [62.0 70.0] $\rm km\,s^{-1}$) is located in a different arm from other parts of the complex (see Table 4).

4 DISCUSSION

4.1 Evolutionary Time in H II Regions and Clump Formation

We searched the NVSS catalog and obtained a total flux of $S_\nu = 4417.0,\ 710.9,\ 796.4$ mJy at $\nu = 1.4$ GHz for the H II regions G018.148–00.283, N22 and N21, respectively (Condon et al. 1998). The flux of stellar Lyman photons $N_{\rm LyC}$, absorbed by the gas in the H II region,

[5] *http://bessel.vlbi-astrometry.org/bayesian*

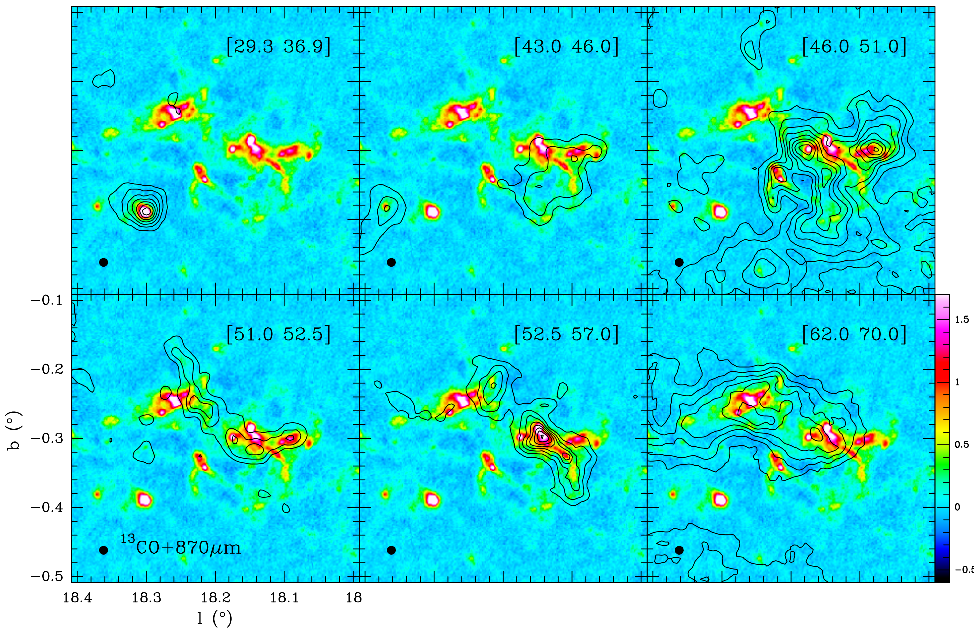

Fig. 6 Integrated-velocity channel maps of ^{13}CO lines superimposed on 870 µm emission for the H II region G18.2–0.3. The integrated velocity ranges are indicated in each panel with the unit of $\mathrm{km\ s^{-1}}$. The contour levels of the ^{13}CO lines start at 3σ in steps of 1σ with $\sigma = 2.08\,\mathrm{K\ km\ s^{-1}}$. The beam size ^{13}CO data is indicated at the bottom-left corner. The unit of the 870 µm color bar is in $\mathrm{Jy\ beam^{-1}}$.

Table 3 The Parameters of the Three Identified Massive Clumps in the Initial Stage

Clump	ΔV (km s^{-1})	Mass ($M_\odot$)	$M_{\rm vir}$ ($M_\odot$)	$\alpha_{\rm vir}$	$t_{\rm clump}$ (Myr)
3	6.09 ± 0.06	405	2804	6.92	1.7
5	3.90 ± 0.08	1243	1310	1.05	2.7
8	6.87 ± 0.12	219	4064	16.59	2.9

Table 4 Different Velocity Components and Distances Associated with G18.2–0.3

Velocity window	1	2	3	4	5	6
Velocity (km s^{-1})	[29.3 36.9]	[43.0 46.0]	[46.0 51.0]	[51.0 52.5]	[52.5 57.0]	[62.0 70.0]
Line center (km s^{-1})	33.10	44.50	48.50	51.75	54.75	66.00
Distance (kpc)	3.22(0.20)	3.36(0.18)	3.40(0.19)	3.45(0.20)	3.52(0.23)	4.92(0.28)
Probability	0.95	1.00	1.00	0.91	0.78	0.64
Spiral arm	ScN	ScN	ScN	ScN	ScN	Nor

can be derived from the relation (Mezger et al. 1974) as

$$\left(\frac{N_{\rm LyC}}{\rm s^{-1}}\right) = \frac{4.761\times10^{48}}{a(\nu,T_{\rm e})}\left(\frac{\nu}{\rm GHz}\right)^{0.1}\left(\frac{T_{\rm e}}{\rm K}\right)^{-0.45} \times\left(\frac{S_\nu}{\rm Jy}\right)\left(\frac{D}{\rm kpc}\right)^2, \quad (7)$$

where $a(\nu, T_{\rm e}) \sim 1$ is a slowly varying function tabulated by Mezger & Henderson (1967), the electron temperature of the H II region is assumed to be $T_e \sim 8000$ K and D is distance. The power exponent of T_e is small, so the result does not depend strongly on the chosen T_e. Based on the above, the derived Lyman-continuum ionizing photon flux and the equivalent stellar class (Panagia 1973) are listed in Table 5.

To check whether the evolutionary status of the H II regions is old enough to trigger a new generation of star formation nearby, we can compare the evolutionary time scales between H II regions and clump formation. We estimate their evolutionary status using the model described by Dyson & Williams (1980) as

$$t_{\rm H\,II} = \frac{4\,R_s}{7\,c_s}\left[\left(\frac{R}{R_s}\right)^{7/4} - 1\right], \quad (8)$$

where R is the radius of H II regions obtained from the NVSS catalog (see Table 5), $c_s = 10\,\mathrm{km\ s^{-1}}$ is the sound

Table 5 The Parameters of the H II Regions

H II	R (pc)	D (kpc)	$S_{1.4\,\mathrm{GHz}}$ (mJy)	$\log(N_{\mathrm{LyC}})$	Stellar Class	$t_{\mathrm{H\,II}}$ (Myr)
G018.148–00.283	0.68	3.52 ± 0.23	4417.0	48.68	O7	2.7
Bubble N22	0.78	4.92 ± 0.28	710.9	48.17	O8.5	4.7
Bubble N21	0.75	3.40 ± 0.19	796.4	47.89	O9.5	5.2

velocity in the ionized gas and R_s is the radius of the Strömgren sphere given by $R_s = (3N_{\mathrm{Lyc}}/4\pi n_0^2 \alpha_B)^{1/3}$, where N_{Lyc} is the number of ionizing photons emitted by the star per second, $n_0 = \sim (1.0 \pm 0.5) \times 10^3\,\mathrm{cm}^{-3}$ is the original ambient density and $\alpha_B = 2.6 \times 10^{-13}\,\mathrm{cm}^3\,\mathrm{s}^{-1}$ is the hydrogen recombination coefficient to all levels above the ground level. Finally, we derive the dynamical age of each H II region, which is also listed in Table 5.

We estimate the fragmentation time of the three early high-mass candidates (clumps 3, 5 and 8) potentially triggered by an H II region nearby according to the theoretical model from Whitworth et al. (1994)

$$t_{\mathrm{clump}} = 1.56 \left(\frac{\alpha_s}{0.2}\right)^{7/11} \left(\frac{N_{\mathrm{Lyc}}}{10^{49}}\right)^{-1/11} \times \left(\frac{n_0}{10^3}\right)^{-5/11} \ [\mathrm{Myr}]\,. \tag{9}$$

The turbulent velocity α_s can be estimated with line width in Table 3. Finally, the derived fragmentation times for the three clumps are listed in Table 3.

Based on derived results in Tables 3 and 5, we find that the evolutionary time of the H II region is longer than the fragmentation time of the three clumps 3, 5 and 8. The fragmentation time is inferred by considering the uncertainty in the total Lyman continuum photon flux and turbulent velocity. Hence, the evolutionary status of the H II regions seems to be responsible for star formation activities around the H II regions.

4.2 Associations of the Initial Stage of Massive Star Formation with the H II Region Nearby

Are the massive clump formations triggered by the H II region nearby in Figure 2? It has been proposed that the formation of H II regions can trigger a new generation of star formation (e.g., Pomarès et al. 2009; Watson et al. 2010). In triggered star formation, one of several events might occur to compress a molecular cloud and initiate its gravitational collapse. Molecular clouds may collide with each other, or a nearby supernova explosion can be a trigger, sending shocked matter into the cloud at very high speeds (Prialnik 2000). The triggered star formation may also happen at the waist of the bipolar H II region (Deharveng et al. 2015), where the high density ionized material flows away from the central region and high density molecular material accumulates to form a torus of compressed material. Ojha et al. (2011) presented an embedded cluster along with three prominent clumps appearing to be sandwiched between the two evolved H II regions S255 and S257, and suggested that the positions of the young sources inside the gas ridge at the interface of the two H II regions favor a site of induced star formation.

Carefully checking the positions (see Sect. 3.6) of the three initial stages of massive star formation, we found that clump Nos. 3 and 8 are located at the border of the western H II region. Maybe clump Nos. 3 and 8 were triggered to be formed by strong stellar winds from the H II region nearby. Clump No. 5 is located at the intersection between two H II regions of bubbles N21 and N22. The case of clump No. 5 is very similar to sandwiched star formation. It is probably that clump No. 5 was born from the compression of the H II regions of bubbles N21 and N22. Therefore, the H II region nearby may be triggering a new generation of star formation, which will be studied in detail in our follow-up works.

4.3 Properties of Associated Massive Star Formation

In Figure 7, we present the mass-size plane for extracted clumps at 870 μm. Comparison with the high-mass star formation threshold of $m(r) > 580\,M_\odot (r/\mathrm{pc})^{1.33}$ empirically proposed by Kauffmann & Pillai (2010) allows us to determine whether these clumps are capable of giving birth to massive stars. The data points are distributed above the threshold (delineated by the line in Fig. 7) that discriminates between high and low mass star formation whose entries fall above and below the line, respectively, indicative of high-mass star-forming candidates. It appears that most of the clumps are high-mass star-forming candidates at 870 μm. Particularly, the potential three initial stages of massive star formation (marked with green crosses) are apparently located above the threshold, suggesting they are high-mass star candidates.

The derived virial masses M_{vir} and virial parameters α_{vir} are listed in Table 3 for the three potential initial stages of massive star formation. Of the three clumps,

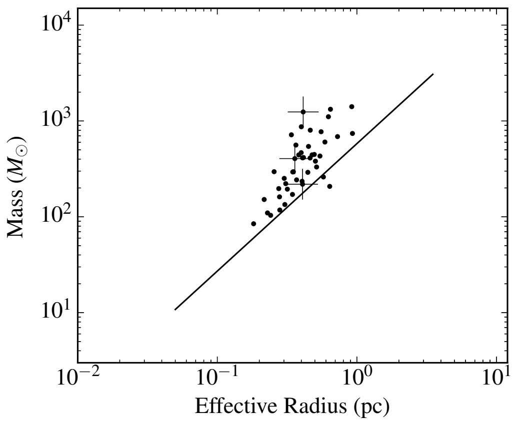

Fig. 7 Mass-radius distributions of Gaussian clumps extracted from *Gaussclumps*. The masses and effective radii are listed in Table 1. The line delineates the threshold $m(r) = 580\ M_\odot (r/pc)^{1.33}$ introduced by Kauffmann & Pillai (2010) separating the regimes under which high-mass stars can form (above) or not (below line). The clump masses in black points (see Table 1) are derived from multiwavelength *Herschel* data. The three crosses indicate the identified potential initial stages (with Nos. 3, 5 and 8 in Table 1) of massive star formation.

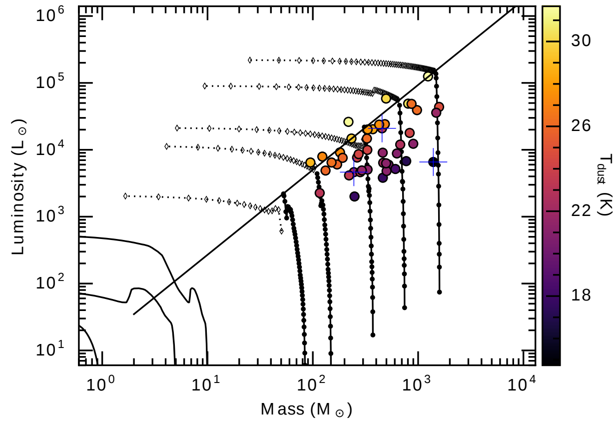

Fig. 8 Luminosity-Mass diagram for sources presented in Table 1. Lines and tracks are from Saraceno et al. (1996) and Molinari et al. (2008), and depict the situation for the low-mass/low-luminosity (below the line) and high-mass/high-luminosity (above the line) regimes. The filled circles with different colors indicate the sources with different dust temperatures. The three blue crosses indicate the identified potential initial stages (with Nos. 3, 5 and 8 in Table 1) of massive star formation.

$\alpha_{\rm vir} > 1$ for clump Nos. 3 and 8, suggesting that the clumps are not gravitationally bound, or in a stable or expanding state, while $\alpha_{\rm vir} < 1$ for clump No. 5, suggesting that the clump is gravitationally bound, potentially unstable and collapsing (Hindson et al. 2013). The interaction within each clump deserves further study, and to understand their initial stages in detail using a higher spatial resolution instrument.

4.4 How to Search for the Initial Stage of Massive Star Formation around an H II Region?

Since H II regions may trigger a new generation of star formation (Churchwell et al. 2007; Churchwell 2008; Watson et al. 2008; Zhang & Wang 2012), it is likely that one can identify early star formation around H II regions. Evidence has shown that star formation in some different evolutionary stages can be found around H II regions, such as starless cores, hot cores, outflows and protostars (Pomarès et al. 2009; Zavagno et al. 2010; Zhang & Wang 2012). Generally an H II region has strong continuum emission at centimeter wavelengths. We can use, e.g. the 21 cm continuum, to trace an H II region. High-mass star formation in the early stage has the properties of being cold, dense and dark. It is well-known that, e.g., the 870 μm continuum has been proposed as one good tracer. Some H II regions, such as hyper-compact H II regions and hot cores, may be deeply embedded in a cold and dense envelope (Zhang et al. 2014), however, they show very low luminosity. These objects do not belong to the initial stage of massive star formation. Therefore, some of these compact clumps at 870 μm are not really in their earliest stage. We need to further remove these clumps with weak centimeter and infrared emissions, and find the relatively early stage of star formation.

In Figure 2, the crosses with numbers are the extracted clumps associated with 870 μm and H II regions. Checking their masses and luminosities in Figure 8, we found that they generally have relatively high masses and low luminosities. In addition, in Figure 7, the mass-size relation shows that most of them are distributed above the high-mass threshold. Particularly in Figure 3 and Table 2, three dense clumps, Nos. 3, 5 and 8 at 870 μm, have weak 24 and 70 μm emission. In other words, these three dense clumps have very weak infrared emission, but with strong emission at 870 μm, so they can be suggested to be infrared quiet clumps. Their dust temperatures for Nos. 3, 5 and 8 are 23.1, 14.7 and 22.2 K (Fig. 4), with masses of 405, 1243 and 219 $M_\odot$, respectively. In Figures 8 and 7, we have highlighted the three clumps with crosses and numbers. Their properties described above suggest that they are potentially in the initial stages of massive star formation.

5 SUMMARY

In previous works, the early stages of star formations were often located within IRDCs. In this work, considering that star formation shows properties of being clustered, the H II region may be triggering a new generation of star formation. It is likely that we can search for the initial stage of massive star formation around H II regions. Therefore, the goal of this work is to present a method of how to search for the initial stage of massive star formation around an H II region.

Towards the H II region G18.2–0.3, we carry out multiwavelength observations to investigate its dust temperature, luminosity, mass, density, the related velocity components and evolution in time. Through analysis, finally we find three (in 45 clump candidates associated with the H II region G18.2–0.3) potential initial stages of massive star formation, suggesting that it is feasible to search for the initial stage of massive star formation around H II regions.

Acknowledgements We wish to thank the anonymous referee for comments and suggestions that improved the clarity of the paper. C.-P. Zhang is supported by the Young Researcher Grant of National Astronomical Observatories, Chinese Academy of Sciences. This work is partly supported by the National Key Basic Research Program of China (973 Program) 2015CB857100, and the National Natural Science Foundation of China 11503035, 11363004 and 11403042. This publication makes use of molecular line data from the Boston University-FCRAO Galactic Ring Survey (GRS). The GRS is a joint project of Boston University and Five College Radio Astronomy Observatory, funded by the National Science Foundation under grants AST-9800334, AST-0098562 and AST-0100793.

References

Aikawa, Y., Herbst, E., Roberts, H., & Caselli, P. 2005, ApJ, 620, 330
André, P., Basu, S., & Inutsuka, S. 2009, Structure Formation in Astrophysics, eds. G. Chabrier (Cambridge: Cambridge University Press), 254
Battersby, C., Ginsburg, A., Bally, J., et al. 2014, ApJ, 787, 113
Battersby, C., Bally, J., Ginsburg, A., et al. 2011, A&A, 535, A128
Benjamin, R. A., Churchwell, E., Babler, B. L., et al. 2003, PASP, 115, 953
Bergin, E. A., & Tafalla, M. 2007, ARA&A, 45, 339
Carey, S. J., Noriega-Crespo, A., Mizuno, D. R., et al. 2009, PASP, 121, 76
Chitsazzadeh, S., Di Francesco, J., Schnee, S., et al. 2014, ApJ, 790, 129
Churchwell, E. 2002, ARA&A, 40, 27
Churchwell, E. 2008, in Astronomical Society of the Pacific Conference Series, 390, Pathways Through an Eclectic Universe, ed. J. H. Knapen, T. J. Mahoney, & A. Vazdekis, 63
Churchwell, E., Povich, M. S., Allen, D., et al. 2006, ApJ, 649, 759
Churchwell, E., Watson, D. F., Povich, M. S., et al. 2007, ApJ, 670, 428
Churchwell, E., Babler, B. L., Meade, M. R., et al. 2009, PASP, 121, 213
Condon, J. J., Cotton, W. D., Greisen, E. W., et al. 1998, AJ, 115, 1693
Csengeri, T., Urquhart, J. S., Schuller, F., et al. 2014, A&A, 565, A75
Cyganowski, C. J., Brogan, C. L., Hunter, T. R., et al. 2014, ApJ, 796, L2
Deharveng, L., Zavagno, A., Samal, M. R., et al. 2015, A&A, 582, A1
Dyson, J. E., & Williams, D. A. 1980, Physics of the Interstellar Medium (New York: Halsted Press)
Egan, M. P., Shipman, R. F., Price, S. D., et al. 1998, ApJ, 494, L199
Evans, II, N. J. 1999, ARA&A, 37, 311
Fuller, G. A., Williams, S. J., & Sridharan, T. K. 2005, A&A, 442, 949
Green, D. A. 2009, Bulletin of the Astronomical Society of India, 37, 45
Griffin, M. J., Abergel, A., Abreu, A., et al. 2010, A&A, 518, L3
Gutermuth, R. A., & Heyer, M. 2015, AJ, 149, 64
Hennebelle, P., & Chabrier, G. 2008, ApJ, 684, 395
Hindson, L., Thompson, M. A., Urquhart, J. S., et al. 2013, MNRAS, 435, 2003
Hofner, P., Delgado, H., Whitney, B., Churchwell, E., & Linz, H. 2002, ApJ, 579, L95
Jackson, J. M., Rathborne, J. M., Shah, R. Y., et al. 2006, ApJS, 163, 145
Jiménez-Serra, I., Caselli, P., Fontani, F., et al. 2014, MNRAS, 439, 1996
Kauffmann, J., Bertoldi, F., Bourke, T. L., Evans, II, N. J., & Lee, C. W. 2008, A&A, 487, 993
Kauffmann, J., & Pillai, T. 2010, ApJ, 723, L7
Kolpak, M. A., Jackson, J. M., Bania, T. M., Clemens, D. P., & Dickey, J. M. 2003, ApJ, 582, 756
Kong, S., Tan, J. C., Caselli, P., et al. 2016, ApJ, 821, 94
Kramer, C., Stutzki, J., Rohrig, R., & Corneliussen, U. 1998, A&A, 329, 249
Lockman, F. J. 1989, ApJS, 71, 469
MacLaren, I., Richardson, K. M., & Wolfendale, A. W. 1988, ApJ, 333, 821
Mezger, P. G., & Henderson, A. P. 1967, ApJ, 147, 471
Mezger, P. G., Smith, L. F., & Churchwell, E. 1974, A&A,

32, 269
Molinari, S., Pezzuto, S., Cesaroni, R., et al. 2008, A&A, 481, 345
Molinari, S., Schisano, E., Elia, D., et al. 2016, A&A, 591, A149
Motte, F., Bontemps, S., Schilke, P., et al. 2007, A&A, 476, 1243
Ojha, D. K., Samal, M. R., Pandey, A. K., et al. 2011, ApJ, 738, 156
Ossenkopf, V., & Henning, T. 1994, A&A, 291, 943
Pagani, L., Lesaffre, P., Jorfi, M., et al. 2013, A&A, 551, A38
Panagia, N. 1973, AJ, 78, 929
Paron, S., Weidmann, W., Ortega, M. E., Albacete Colombo, J. F., & Pichel, A. 2013, MNRAS, 433, 1619
Perault, M., Omont, A., Simon, G., et al. 1996, A&A, 315, L165
Pillai, T., Caselli, P., Kauffmann, J., et al. 2012, ApJ, 751, 135
Pillai, T., Kauffmann, J., Wyrowski, F., et al. 2011, A&A, 530, A118
Pillai, T., Wyrowski, F., Carey, S. J., & Menten, K. M. 2006, A&A, 450, 569
Pillai, T., Wyrowski, F., Hatchell, J., Gibb, A. G., & Thompson, M. A. 2007, A&A, 467, 207
Poglitsch, A., Waelkens, C., Geis, N., et al. 2010, A&A, 518, L2
Pomarès, M., Zavagno, A., Deharveng, L., et al. 2009, A&A, 494, 987
Prialnik, D. 2000, An Introduction to the Theory of Stellar Structure and Evolution (Cambridge: Cambridge University Press)
Rathborne, J. M., Jackson, J. M., Chambers, E. T., et al. 2010, ApJ, 715, 310
Rathborne, J. M., Simon, R., & Jackson, J. M. 2007, ApJ, 662, 1082
Reid, M. J., Dame, T. M., Menten, K. M., & Brunthaler, A. 2016, ApJ, 823, 77
Russeil, D., Zavagno, A., Motte, F., et al. 2010, A&A, 515, A55
Sanhueza, P., Jackson, J. M., Foster, J. B., et al. 2012, ApJ, 756, 60
Saraceno, P., Andre, P., Ceccarelli, C., Griffin, M., & Molinari, S. 1996, A&A, 309, 827
Schuller, F., Menten, K. M., Contreras, Y., et al. 2009, A&A, 504, 415
Stutzki, J., & Guesten, R. 1990, ApJ, 356, 513
Tan, J. C., Kong, S., Butler, M. J., Caselli, P., & Fontani, F. 2013, ApJ, 779, 96
Traficante, A., Calzoletti, L., Veneziani, M., et al. 2011, MNRAS, 416, 2932
Walsh, A. J., Hyland, A. R., Robinson, G., & Burton, M. G. 1997, MNRAS, 291, 261
Wang, K., Testi, L., Ginsburg, A., et al. 2015, MNRAS, 450, 4043
Wang, K., Zhang, Q., Wu, Y., & Zhang, H. 2011, ApJ, 735, 64
Wang, K., Zhang, Q., Testi, L., et al. 2014, MNRAS, 439, 3275
Watson, C., Hanspal, U., & Mengistu, A. 2010, ApJ, 716, 1478
Watson, C., Povich, M. S., Churchwell, E. B., et al. 2008, ApJ, 681, 1341
Whitworth, A. P., Bhattal, A. S., Chapman, S. J., Disney, M. J., & Turner, J. A. 1994, MNRAS, 268, 291
Wyrowski, F. 2008, in Astronomical Society of the Pacific Conference Series, 387, Massive Star Formation: Observations Confront Theory, ed. H. Beuther, H. Linz, & T. Henning, 3
Yuan, J.-H., Wu, Y., Li, J. Z., & Liu, H. 2014, ApJ, 797, 40
Zavagno, A., Anderson, L. D., Russeil, D., et al. 2010, A&A, 518, L101
Zhang, C. P., & Wang, J. J. 2012, A&A, 544, A11
Zhang, C.-P., & Wang, J.-J. 2013, RAA (Research in Astronomy and Astrophysics), 13, 47
Zhang, C.-P., Wang, J.-J., & Xu, J.-L. 2013, A&A, 550, A117
Zhang, C.-P., Wang, J.-J., Xu, J.-L., Wyrowski, F., & Menten, K. M. 2014, ApJ, 784, 107
Zhang, C.-P., Yuan, J.-H., Li, G.-X., Zhou, J.-J., & Wang, J.-J. 2017, A&A, 598, A76
Zhang, C.-P., Li, G.-X., Wyrowski, F., et al. 2016, A&A, 585, A117